RESEARCH ARTICLE

Key Points:
- Alongshore transport of plume water occurs in initial stage of upwelling development, while offshore transport in mature stage
- The baroclinic effect is important to intensifying the horizontal velocity at the upwelling front and freshwater transport
- Offshore movement of the high PGF zone due to Ekman transport and shift of upwelling front is responsible for the change in plume pathways

Correspondence to:
W. Gong,
gongwp@mail.sysu.edu.cn

Development of upwelling on pathway and freshwater transport of Pearl River plume in northeastern South China Sea

Zhaoyun Chen[1,2] (ID), Yuwu Jiang[3], James T. Liu[4] (ID), and Wenping Gong[1,2] (ID)

[1]School of Marine Sciences, Sun Yat-sen University, Guangzhou, China, [2]Guangdong Provincial Key Laboratory of Marine Resources and Coastal Engineering, Guangzhou, China, [3]State Key Laboratory of Marine Environmental Science, Xiamen University, Xiamen, China, [4]Department of Oceanography, National Sun Yat-sen University, Kaohsiung, Taiwan

Abstract In situ observations, satellite images, and numerical modeling results have shown that the Pearl River plume axis extends alongshore and passes through two separate upwelling regions—one off the Guangdong and Fujian coasts (the Yuedong upwelling) and the other in the Taiwan Bank during the initial and medium stages of the Yuedong upwelling, while it is directed offshore when the Yuedong upwelling is strong. Model experiments are conducted to examine the effects of wind strength and baroclinicity on the upwelling and the corresponding pathway and freshwater transport of the Pearl River plume. The baroclinic effect is important to intensifying the horizontal velocity at the upwelling front and freshwater transport in the northeastern South China Sea. The freshwater transport flux is further decomposed into advection, vertical shear, and tidal pumping components, and advection is the dominant contributor. As the Yuedong upwelling develops, the zone with a relatively high-pressure gradient moves offshore due to offshore Ekman transport and the shift in the upwelling front, which is responsible for the offshore transport of the river plume. When the river plume is transported to the outer-shelf, sometimes it can be further entrained into eddies, allowing its export to the open sea.

1. Introduction

The variations of the East Asian monsoon and the interactions of different currents with submarine topography result in complex hydrodynamics and water masses in the northeastern South China Sea (SCS) during summer. The southwesterly monsoon prevails in June and July, and the average wind stress is weaker than 0.025 N m^{-2} [*Jan et al.*, 2002]. Water masses from the river plume and upwellings of different intensities are detected in the northeastern SCS from summer cruises [*Hu et al.*, 2011]. Three current systems occupy the southern Taiwan Strait in summer, and the combined volume transport through the Taiwan Strait is approximately 2.3 × 10^6 m^3 s^{-1}, which contributes substantial buoyant water and water-borne materials from the SCS to the East China Sea [*Hu et al.*, 2010].

Figure 1a shows the bathymetric contours in the northeastern SCS. The shelf widens eastward, with the 50 m isobath extending from 50 km offshore at 116°E to 150 km offshore at 119°E. A shallow shoal, the Taiwan Bank, is located on the widened shelf off Dongshan Island. A deep channel, the Penghu Channel, is located along the east of the Taiwan Strait, which facilitates northward transport of SCS water in summer. A schematic diagram of the major currents in the northern SCS during summer is presented in Figure 1b. The SCS warm current flows persistently northeastward and straddles the shelf break region [*Su*, 2004]. Part of this warm current extends northeastward through the Taiwan Strait, with the Yuedong coastal current on its left and the extension of the Kuroshio Loop Current on its right [*Hu et al.*, 2010]. After the Pearl River effluent enters the shelf region, it can be forced northeastward by the Yuedong coastal current and the southwesterly monsoon, which was confirmed by in situ observations of low-salinity water from the Pearl River in the northeastern SCS during summer 2005 [*Hong et al.*, 2009].

The upwelling off the Guangdong and Fujian coasts (the Yuedong upwelling) has received considerable attention in recent years for its distribution and physical mechanisms. In situ observations show the upwelling off the coast between Dongshan Island and Shantou [e.g., *Hu et al.*, 1999; *Hong et al.*, 2009]. Remote sensing data also confirm this upwelling by its relatively low sea surface temperature (SST) and high level of chlorophyll-*a*. The upwelling is strong in July and decays after the middle of August [*Tang et al.*, 2002; *Cai*
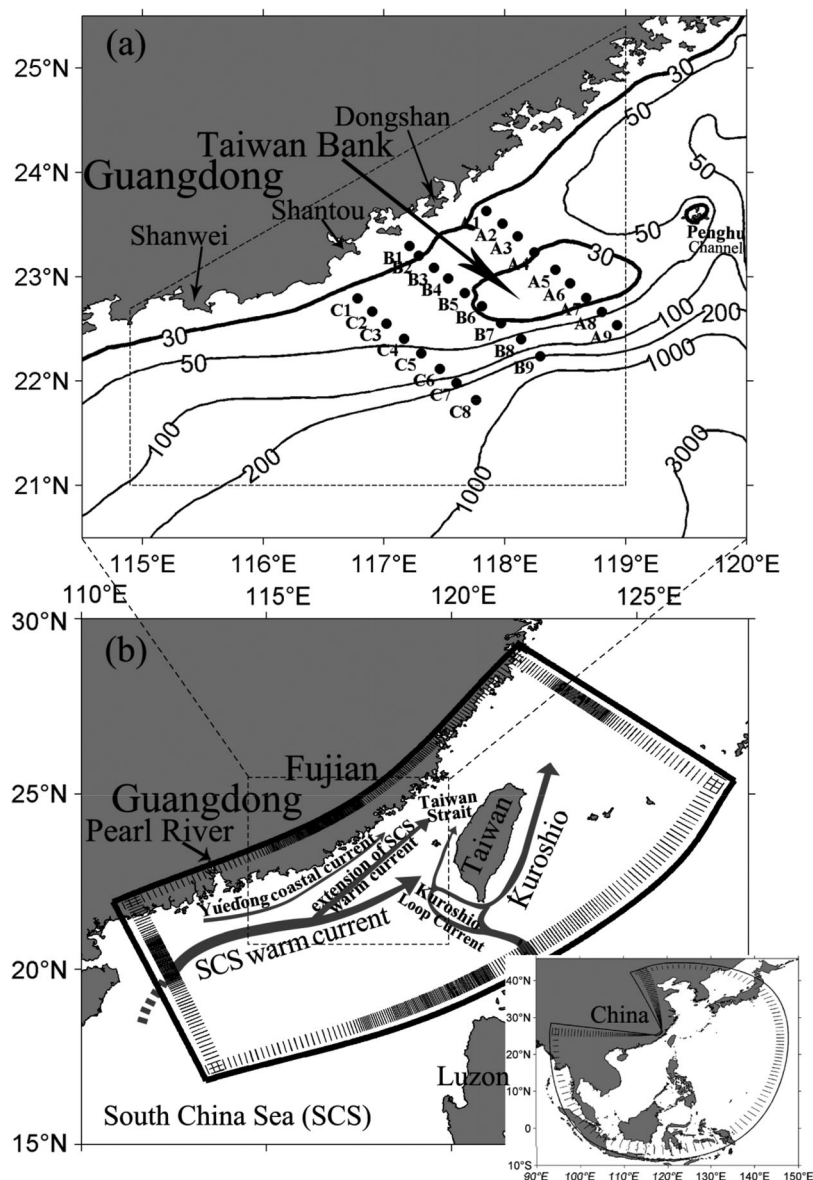
Figure 1. (a) Bathymetry in the northeastern SCS (contours; in m). Black dots mark the CTD stations: A1–A9, B1–B9, and C1–C8. Black dash line encircles a region, where wind is reduced in numerical model experiment for Case B. (b) Fine-grid model domain for the study region. The bottom right inset shows the coarse-grid model domain. The boundary lines are ticked every three grids for the fine-grid domain and every four grids for the coarse-grid domain. Note that the grids are denser over the shelf in the northeastern SCS. The major currents in summer are also presented in arrows, which are redrew from *Hu et al.* [2010].

et al., 2011]. It has been suggested that the widened shelf and coastal promontory are responsible for the intensified Yuedong upwelling [*Gan et al.*, 2009a]. Upwelling-favorable wind and the interaction between large-scale currents and topography are the two key factors that trigger this upwelling [*Wang et al.*, 2012; *Wang et al.*, 2014].

Hu et al. [2003] reviewed the upwelling in the Taiwan Bank and noted that a belt-like upwelling existed year-round. Observations show that the upwelling is located at the southeastern edge of the Taiwan Bank; the temperature drops 2.5–3.5°C at the surface, and its size and intensity vary over time [*Tang et al.*, 2002; *Hu et al.*, 2011]. Interaction of the year-round northeastward extension of the SCS warm current with the topography can bring the cold subsurface water to a depth of approximately 25 m at the edge of the Taiwan Bank, and strong tidal mixing forces it further upward to the surface [*Jiang et al.*, 2011]. Tidal mixing and the ascending bottom current at the edge of the Taiwan Bank are thought to generate the upwelling in the Taiwan Bank [*Hu et al.*, 2003; *Jiang et al.*, 2011].

Many studies have been conducted on the dynamics of the Pearl River plume. It is commonly known that a two-layer gravitational circulation prevails in the Pearl River Estuary, and the plume front and spread are largely determined by the winds and tides [e.g., *Wong et al.*, 2003; *Pan et al.*, 2014; *Zu et al.,* 2014]. Off the Pearl River Estuary, the dispersal of the Pearl River plume has four patterns: bulge, westward spreading, eastward spreading, and alongshore symmetrical spreading, as determined by the wind and coastal current [*Ou et al.*, 2009]. When it is advected eastward off the Guangdong coast, the plume thins in the surface layer, and cross-shore circulation is enhanced in the upper water column [*Gan et al.*, 2009b]. The eastward plume water reaches the southern Taiwan Strait and has little effect on the upwelling circulation near the bottom [*Shu et al.*, 2011]. This low-salinity plume water can even be detected in the Penghu Channel [*Bai et al.*, 2015]. The plume water enhances the water stratification and alongshore current by approximately 0.2 m s^{-1} [*Shu et al.*, 2014].

The river plume structures over the continental shelf are affected by winds, coastal currents, and tides. As the river plume resides at the surface, it is susceptible to the surface Ekman effect. Upwelling-favorable winds drive the plume offshore and mixing persists at the seaward plume front; a downwelling-favorable wind drives the plume onshore and the plume thickness increases [*Fong and Geyer*, 2001; *Choi and Wilkin*, 2006]. The ambient flow over the shelf can also alter the direction and magnitude of the freshwater transport [*García-Berdeal et al.*, 2002]. The plume front over the shelf is modulated by the spring-neap variations of the tidal mixing, and the spatial distribution of the river plume also varies through the spring-neap tidal circles [*Geyer*, 1995; *Wu et al.*, 2011].

Freshwater transport associated with the river plume is largely influenced by the coastal dynamics. Modeling results have shown that the seasonal patterns of freshwater transport from the Mississippi River are consistent with the prevailing winds and that the freshwater is pooled up the coast during the summer due to upwelling-favorable winds and down the coast in nonsummer months due to downwelling-favorable winds [*Zhang et al.*, 2012]. *Kim et al.* [2014] also found that the freshwater flux in the Korea Strait transported from the Changjiang River discharge was related to the southeasterly wind during summer. External forcing facilitates the transport of freshwater downstream; for example, the ambient current augments the downstream freshwater transport [*Fong and Geyer*, 2002]. Tidal currents can compress the bulge shoreward and enhance the down-shelf current, thus increasing freshwater transport in the downstream coastal currents [*Li and Rong*, 2012; *Chen*, 2014].

Although upwelling and river plume dynamics have received considerable attention in recent years, the effects of upwellings on the buoyant river plume are not well understood. In particular, little is known about the dynamic response of the river plume to the development of an upwelling. A study of the influence of the upwelling on the dynamics of the river plume should help us to better understand the spatial distribution of the plume water and the fate of river-borne materials, which are important to coastal sedimentation and biological activities. The aims of this paper are (1) to examine wind and baroclinic effects on the pathway of upwelling-related river plume dispersal in the northeastern SCS; (2) to quantitatively determine the corresponding freshwater transport and depth-integrated fluxes; and (3) to explore the mechanisms of offshore freshwater transport when the upwelling develops. The remainder of this paper is organized as follows. The observation data and model descriptions are introduced in section 2. Comparisons of the modeling results with the observations, model experimental results, and freshwater transport analysis are presented in section 3, followed by a discussion in section 4 and our conclusions in section 5.

2. Methods

2.1. In Situ Observations

A hydrographic cruise survey was conducted in the northeastern SCS during the summer of 2011. Only the temperature and salinity data gathered from 30 June to 4 July are used in this study. A Sea-bird SBE 917plus CTD was used to measure the temperature and salinity in three transects (shown by black dots in Figure 1a). A shipboard SBE 21 Thermosalinograph was used to implement the underway measurements of surface temperature and salinity every 5 s along the cruise route (shown by a black line in Figure 2a). The survey covers the widened shelf off the Guangdong coast, where the upwelling occurs frequently during summer. The downcast data at the stations are interpolated to plot the depth profiles of temperature and salinity along each transect using the Kriging interpolation method, which is also applied to plot the
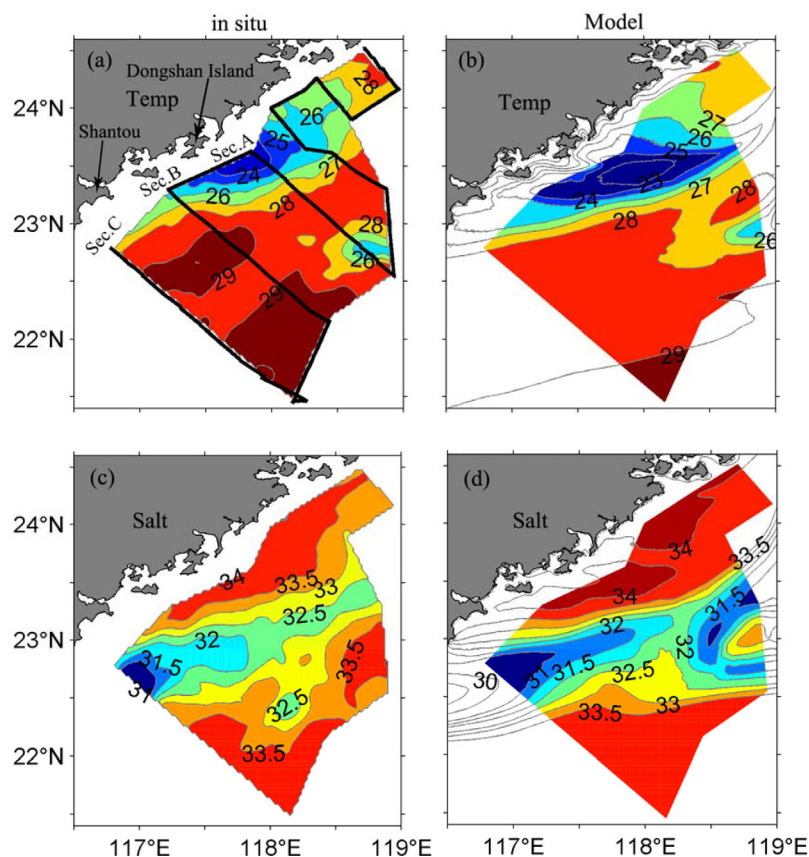
Figure 2. Surface temperature (°C) from (a) in situ observations and (b) model results. Black line in Figure 2a shows the cruise survey transection from 30 June to 4 July 2011. Surface salinity from (c) in situ observations and (d) model results. Model results are 5 day averaged from 30 June to 4 July.

underway surface distributions of temperature and salinity. The observation data are used to characterize the spatial distributions of the upwelling and the river plume and to validate the numerical modeling results.

2.2. Remote Sensing Data

The Moderate Resolution Imaging Spectroradiometer (MODIS) level 2 SST data in July 2011 with a 1 km resolution are used to delineate the upwelling regions with a relatively low temperature, which are downloaded from NASA's OceanColor website (http://oceancolor.gsfc.nasa.gov/). The turbidity data with a 1 km resolution are derived from the MODIS level 2 normalized water-leaving radiances at 667 and 488 nm bands [*Huang et al.*, 2008]. This turbidity algorithm has been successfully used to study the dispersal of the Pearl River plume in the northern SCS [*Chen et al.*, 2016]. The turbid plume water is easily distinguished from the clear seawater, so the river plume's pathway can be captured by the satellite turbidity images.

All-satellite-merged gridded sea level anomaly (SLA) with 0.25° resolution in delayed time by Ssalto/Duacs were downloaded from the AVISO website (http://www.aviso.altimetry.fr/). The sea surface geostrophic currents were derived from the SLA data set and used to detect eddies in the northern SCS.

2.3. Numerical Modeling
2.3.1. Model Configurations

The Regional Ocean Modeling System (ROMS; http://www.myroms.org) is used to study the upwelling and related plume dynamics and to quantify the freshwater transport. It is a three-dimensional, free-surface, terrain-following ocean model that solves the hydrostatic primitive equations on a staggered Arakawa C-grid [*Shchepetkin and McWilliams*, 2005]. We applied this model to explore the upwelling processes and

Table 1. Numerical Experiments Scenarios

Experiments	Description
Case A	Normal
Case B	Tenth wind strength
Case C	Barotropic

mechanisms in the northern Taiwan Strait [*Chen et al.*, 2014]. More details on the model configurations were given by *Lin et al.* [2016]. Some brief descriptions are given as follows.

The coarse-grid model domain covers the SCS and the northwestern Pacific, and the grids are concentrated in the Taiwan Strait (bottom right inset in Figure 1b). The fine-grid model domain covers the northeastern SCS and the Taiwan Strait (Figure 1b). We use a one-way nesting method, in which the initial and boundary conditions of the temperature, salinity, currents, and surface elevations in the fine-grid model are interpolated from the 5 year simulation of the coarse-grid model results. The Clamped and Flather boundary conditions are used on the open boundaries. The vertical turbulent viscosity and diffusivity are computed with the Large McWilliams and Doney (LMD) shear-mixing scheme [*Large et al.*, 1994]. The bottom stress is calculated by a logarithm with a bottom roughness height of 3×10^{-3} m. Ten major tidal constituents (M_2, S_2, N_2, K_2, K_1, O_1, P_1, Q_1, M_f, and M_m) derived from TPXO 7.0 are incorporated in the model [*Egbert and Erofeeva*, 2002]. The climatological surface heat flux from the Comprehensive Ocean-Atmosphere Data Set (COADS) 2005 is forced on the surface.

The coarse-grid model is configured with 400×400 grid cells in orthogonal curvilinear coordinate and 30 vertical terrain-following *s*-levels. The initial and boundary conditions of the temperature and salinity are interoperated from the World Ocean Atlas (WOA) 2009. The climatological monthly mean QuikSCAT winds, with 0.25° resolution, are forced on the sea surface.

The fine-grid model is configured with 300×600 grid cells in orthogonal curvilinear coordinate and 25 vertical *s*-levels with refinement in the surface layers. The grid resolution increases in the northeastern SCS (~1 km). The 6 hourly cross-calibrated multiplatform (CCMP) winds with 0.25° resolution derived from the SeaWinds measurements (http://podaac.jpl.nasa.gov) are forced on the sea surface. The constant climatological-mean Pearl River discharge in summer ($Q_0 = 1.82 \times 10^4$ m^3 s^{-1}) with zero salinity and a temperature of 30°C is added as the lateral boundary condition [*Zhao*, 1990]. The fine-grid model was run from 1 April to 30 July 2011, and hourly model results are output for further analysis.

2.3.2. Experiment Settings

Table 1 summarizes the numerical model experiments in the fine-grid model. Case A is a normal run, in which the CCMP wind, tides, baroclinic effect, river discharge, and surface heat flux are included in the model. In Case B, the wind strength in the upwelling regions (bordered by a dashed line in Figure 1a) is reduced to one tenth of that in Case A from 24 June to 30 July, and the wind direction is kept the same. In Case C, the baroclinic effect is removed, that is, the pressure gradient induced by the density difference is omitted. The density still has spatiotemporal variations, which can act upon the mixing. This method was used by *Wong et al.* [2003] to examine the baroclinic effect on the plume and frontal dynamics in the Pearl River Estuary. We designate Case C as the barotropic case. Cases B and C are the control experiments. Compared with Case A, an individual forcing agent is altered in Cases B and C, respectively.

3. Results

3.1. Observations and Model Results

The observed underway surface temperature is shown in Figure 2a. The Yuedong upwelling with a relatively low temperature develops off the coast. The upwelling core is located off Dongshan Island, and the low-temperature water extends approximately 100 km offshore. Compared with the surrounding nonupwelling water, the surface temperature drops at least 4°C in the upwelling core. Another cold upwelling region exists in the Taiwan Bank, where the temperature drops 1–3°C. Only part of this upwelling is captured in the observation. The average temperature from 30 June to 4 July at the surface layer from the modeling results is given in Figure 2b. The modeled surface temperature shows good correspondence with the in situ observations. The two upwelling regions are reproduced by the model, although the Yuedong upwelling is slightly stronger in the model than in the observations.

The salinity field shows that low-salinity water extends to the northeastern SCS, and the main axis passes through the two separate upwelling regions, while a part of it leaks offshore (Figure 2c). This low-salinity water originates from the Pearl River, which travels more than 400 km to the northeastern SCS [*Hong et al.*, 2009]. The salinity is less than 31 psu at 117°E and gradually increases northeastward. The relatively low-

salinity signal is also detected east of the Taiwan Bank. Low-salinity water is distributed adjacent to the upwelling regions (Figures 2a and 2c). The model results present similar pathways where the northeastward Pearl River plume axis passes through the two upwelling regions, and some of the plume water travels eastward (Figure 2d). The difference between the in situ observations and the model results is likely due to conditions such as the constant Pearl River discharge, the climatological surface heat flux, and the climatological boundary conditions adopted in the model.

Figure 3 compares the vertical structures of temperature and salinity along transects A–C (Figure 1a). The observed temperature structures show the remarkable Yuedong upwelling and the upwelling in the Taiwan Bank. The strong Yuedong upwelling causes vertical homogeneous temperature structures along A1 through A4, and the temperature increases offshore (shown by the red line in Figure 3a). The outcrop of 26–28 isotherms between Stations A6 and A8 demonstrates the upwelling at the edge of the Taiwan Bank. The 25–27 isotherms tilt upward toward the shore and outcrop near the shore in Sections B and C (Figures 3c and 3e). The upwelling can bring cold subsurface water from a depth of 40 m to the surface.

The observed salinity fields show that two separate low-salinity lenses appear in Sections A and B (Figures 3b and 3d): one between the two upwelling regions approximately 75 km from the A1 (B1) station, and the other approximately 145 km from the station. The plume is 5 m thick in Section A and 20 m thick in Section B on the surface. The entire water column near the shore is occupied by the relatively low-salinity water in Section C (Figure 3f). The low-salinity water lens is separated into two parts from Section C to Section A. Plume water with a salinity of less than 32 psu is present in all three sections and reaches a width of approximately 40 km on the surface.
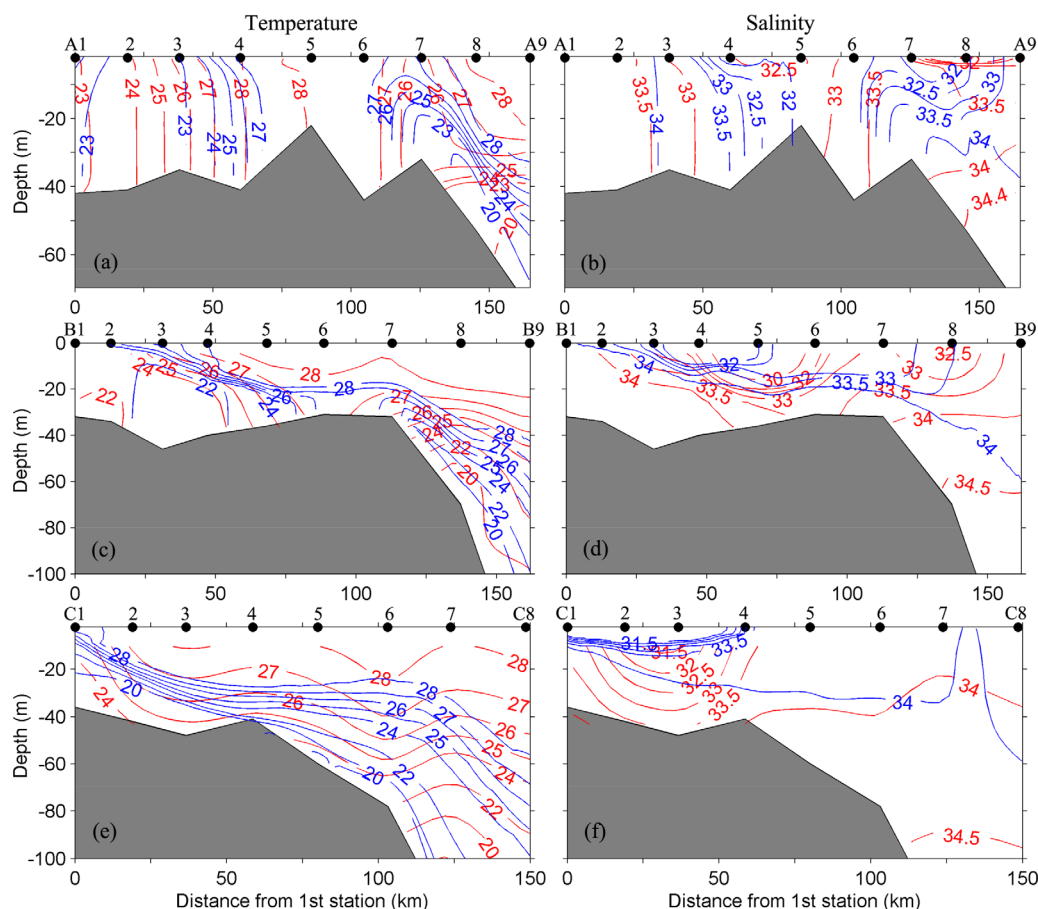
Figure 3. Depth profiles of temperature (°C) in (a) Section A, (c) Section B, and (e) Section C. Depth profiles of salinity (psu) in (b) Section A, (d) Section B, and (f) Section C. Observed and modeled results are shown in red and blue lines, respectively. Locations of the CTD stations are shown in Figure 1a.

The model captures the main features of the upwelling and the adjacent river plume dispersal, including the well-mixed water in the coastal upwelling region in Section A, the outcrop of subsurface water in the Taiwan Bank, the upward and shoreward tilting of the isotherms in Sections B and C, and the offshore movement of the surface plume water from Section C to Section A.

To examine the effects of the wind on the upwelling and the associated river plume dispersal, we plot a stick diagram of the daily winds in June and July 2011, averaged in the coastal region (bordered by the dashed line in Figure 1a) from the CCMP wind data set (Figure 4a). The wind shifts back and forth before 24 June, and upwelling-favorable wind prevails for a month thereafter. The wind speed varies from 4 to 15 m s^{-1}.

The MODIS SST in the northeastern SCS on 4 July is portrayed in Figure 4b. A moderate upwelling develops from 116°E to 118.5°E off the coast. An upwelling with a relatively low temperature extends approximately 60 km offshore, and the temperature decreases by more than 2.5°C in the upwelling core. Turbid plume water stretches northeastward along the Yuedong upwelling front, and some plume water travels eastward to the east of the Taiwan Bank (Figure 4d). In the figure, the turbid areas induced by the upwelling (coder than 28.6°C) and the low-turbidity areas (<0.04 NTU) in the open sea are blanked. The remaining pixels roughly depict the spatial distribution of the river plume. The turbid river plume (>2 NTU) is advected to 116°E and extends to the southern Taiwan Strait, maintaining a turbidity of 0.3 NTU. The model results reproduce the Yuedong upwelling (Figure 4c). The modeled surface temperature is lower than the MODIS SST, probably due to the climatological heat flux used in the model. A belt-like upwelling forms in the Taiwan Bank, which is the same to the previous study [*Hu et al.*, 2003]. The corresponding modeled surface salinity and currents are displayed in Figure 4e. The Pearl River plume is advected alongshore near the coast and departs from the coast at 116°E. The coastal currents bring it further northeastward. Some of the plume water is sandwiched between the two upwelling regions, and some veers to the east of the Taiwan Bank. The distribution of plume water is similar to that observed in the satellite turbidity image (Figure 4e versus 4d).
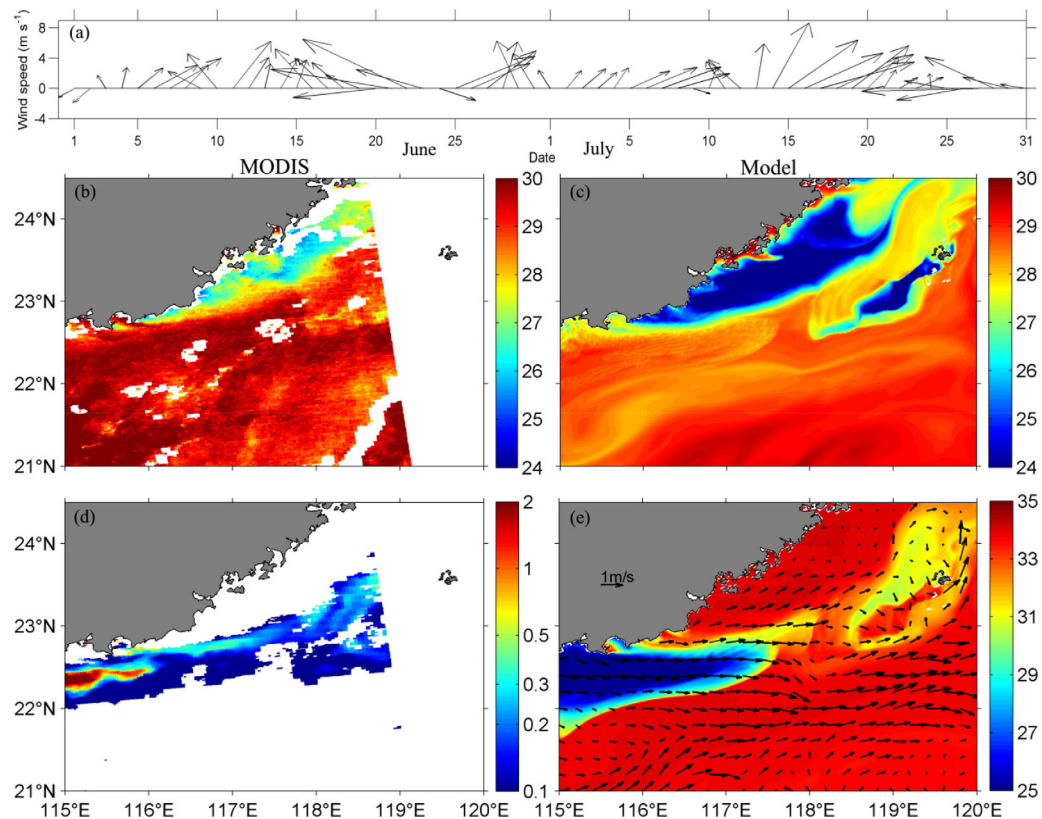
Figure 4. (a) Stick diagram of the CCMP wind velocity (m s^{-1}) in June and July 2011. SST (°C) at 6:10 UTC, 4 July 2011 from (b) the MODIS, and (c) model results. (d) The corresponding turbidity (NTU) image from the MODIS, where low-temperature or low-turbidity areas are blanked. (e) The corresponding modeled surface salinity (psu; color shading) and currents (m s^{-1}; vectors).
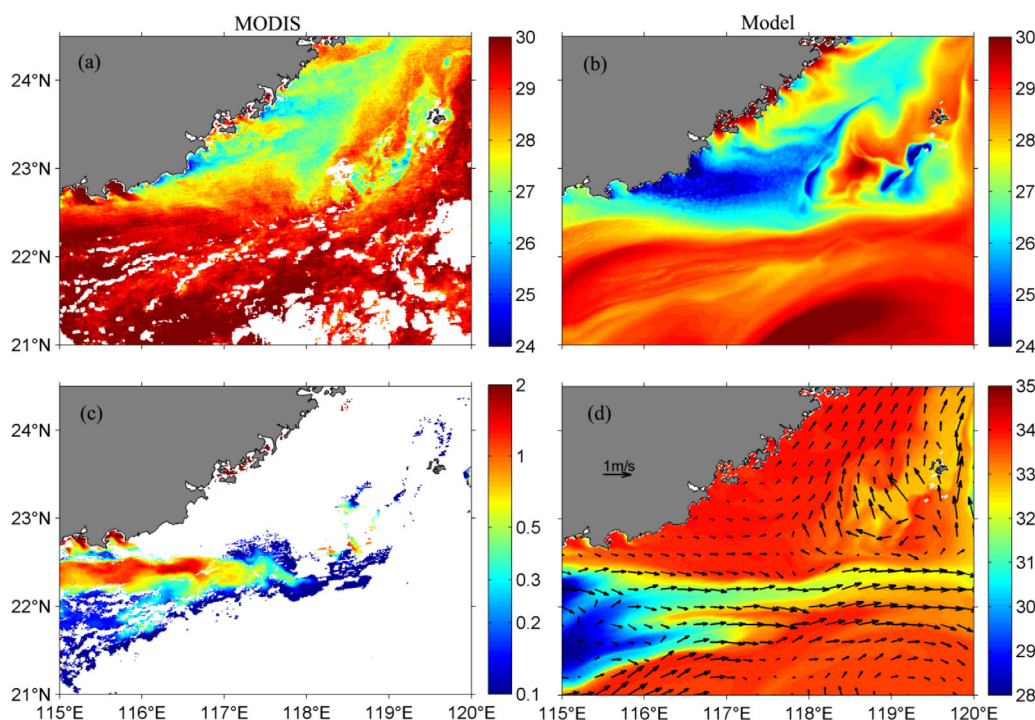
Figure 5. Same as Figures 4b–4e, but for 5:45 UTC, 24 July 2011.

After the intermittent upwelling-favorable wind blows for another 20 days, the Yuedong upwelling is fully developed on 24 July (Figure 5a). Two upwelling cores are located off Dongshan Island and Shantou. The Yuedong upwelling extends approximately 120 km offshore and nears the upwelling in the Taiwan Bank. The fully developed Yuedong upwelling closes the alongshore transport conduit for the plume water between the two upwelling regions when the Yuedong upwelling is at moderate strength, as shown in Figure 4. Accordingly, the turbid plume water is advected eastward until east of the Taiwan Bank, approximately 200 km offshore (Figure 5c). The turbid water, with a width of 40 km, remains above 0.5 NTU until it reaches 117°E. The model results reproduce the fully developed Yuedong upwelling, which is near the upwelling in the Taiwan Bank, and the eastward offshore transport of the plume water observed in the satellite images (Figure 5).

3.2. Model Experiments

After the model results are verified by the in situ observations and remote sensing data, the model is used to conduct several numerical experiments and to examine the wind strength and baroclinic effects on the upwelling and on the related plume dynamics. The cases on 26 June and 8 July are selected as two scenarios in the initial and mature stages of the upwelling, when the periodic upwelling-favorable wind blows for 2 days and for 10–12 days. We check the dispersals of the river plume in response to different upwelling intensities influenced by the forcing agents.

The surface temperature on 26 June in Case A shows that the weak Yuedong upwelling develops off the coast, and a belt-like upwelling is seen in the Taiwan Bank (Figure 6a). The temperature drops by approximately 2°C in the upwelling regions. At the same time, the Pearl River plume spreads eastward near the coast west of 116.5°E and is then directed northeastward off the Yuedong upwelling (Figure 6b). The plume axis is distributed in the nonupwelling area between these two upwelling regions. Some of the plume water is brought to the east of the Taiwan Bank and finally flows northward through the Penghu Channel.

When the upwelling-favorable wind forcing is reduced to one tenth of its intensity after 24 June in Case B, the Yuedong upwelling is not evident on the surface on 26 June (Figure 6c). Compared with Case A, the pathway of the river plume approaches nearer the coast east of 116.5°E, because of the weaker offshore
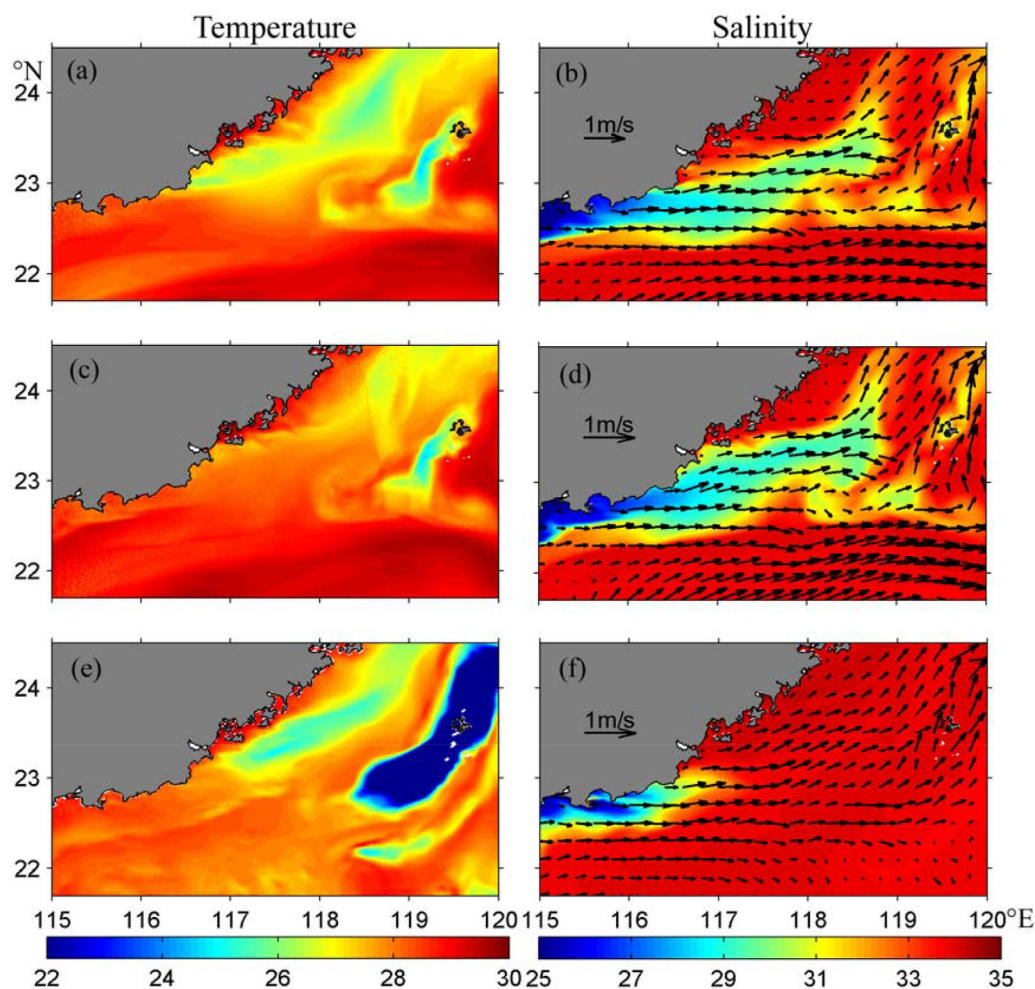
Figure 6. Surface temperature (°C) on 26 June 2011 for (a) Case A, (c) Case B, and (e) Case C. Right column shows the corresponding surface salinity (psu; color shading) and currents (m s^{-1}; vectors).

Ekman currents and Yuedong upwelling (Figure 6d). The plume axis is located west of the upwelling in the Taiwan Bank.

When the baroclinic effect is removed in Case C, the upwelling in the Taiwan Bank is largely intensified, whereas the Yuedong upwelling changes little compared with Case A (Figure 6e). The subsurface water with a temperature lower than 22°C is stirred to the surface by the tide-induced mixing in the Taiwan Bank. The northeastward extending river plume is reduced remarkably (Figure 6f). The low-salinity tongue reaches only 117°E, and the plume water remains near the coast.

When the prevailing upwelling-favorable wind blows for 10–12 days, a strong Yuedong upwelling develops off the coast on 8 July in Case A, approximately 100 km wide and 300 km long (Figure 7a). The Yuedong upwelling is stronger than that on 26 June, and the tide-induced upwelling in the Taiwan Bank changes little. The Pearl River plume that arrives at the south edge of the Yuedong upwelling is mostly advected eastward to the east side of the Taiwan Bank at least 200 km offshore (Figure 7b). The river plume's main pathway changes from alongshore on 26 June to offshore on 8 July. A small amount of the river plume remains between the two upwelling regions.

Compared with Case A, the weaker prevailing upwelling-favorable wind causes a weaker Yuedong upwelling on 8 July in Case B (Figure 7c). Patches of upwelling develop off the coast. The Pearl River plume is advected northeastward off the Yuedong upwelling and bifurcates at the head of the upwelling in the Taiwan Bank (Figure 7d). One moves along the Yuedong upwelling front, sandwiched between the two
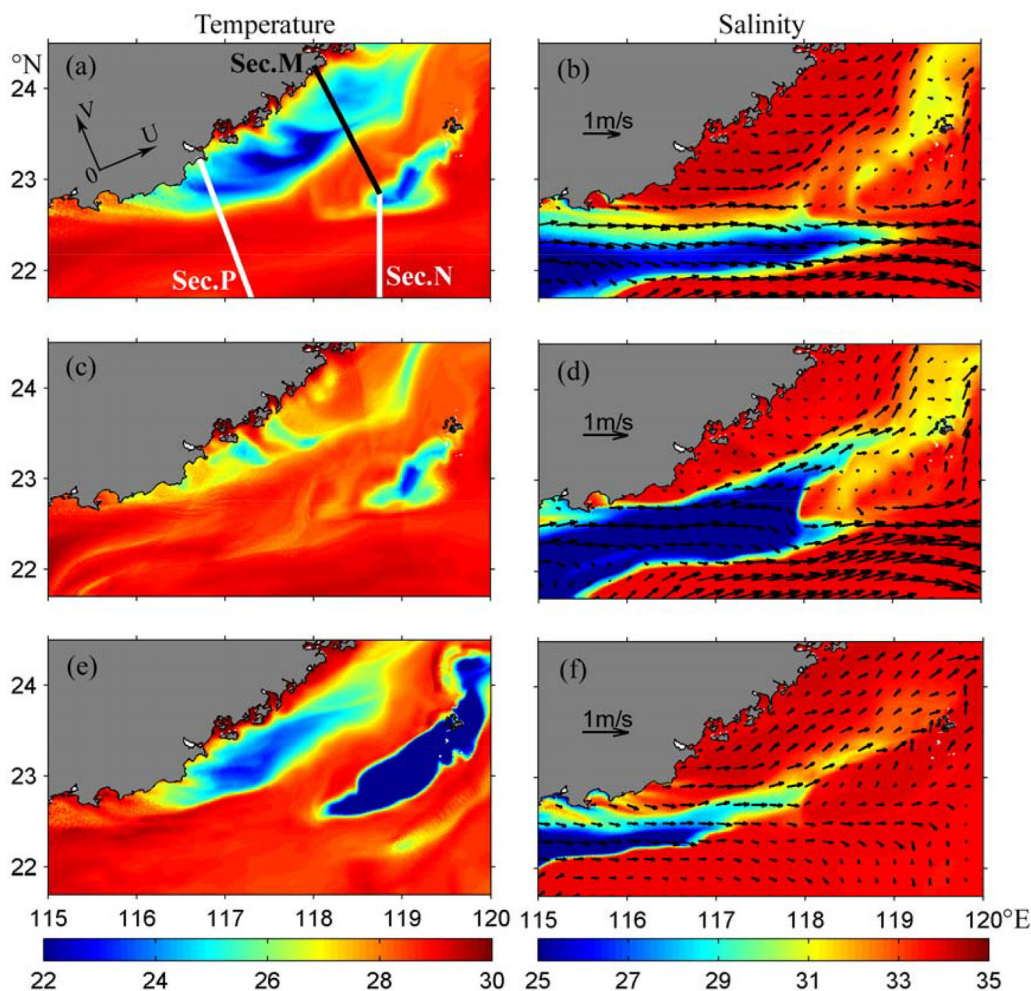
Figure 7. Same as Figure 6, but for 8 July 2011. Lines in Figure 7a mark Sections M and N for computing freshwater transport in Figure 8, and Section P for mechanisms analysis in Figures 11 and 12.

upwelling regions, and the other tends to divert eastward. Unlike Case A, in which most of the plume water travels offshore, the lower wind strength and offshore Ekman transport in Case B result in a weaker Yuedong upwelling, accompanied by greater alongshore freshwater transport between the two upwelling regions. The development of a coastal upwelling on 8 July drives the river plume further offshore than on 26 June (Figure 6d versus 7d).

In Case C, on 8 July, the Yuedong upwelling is weaker and the upwelling in the Taiwan Bank is stronger than that in Case A (Figure 7e). These findings suggest that the baroclinic effect is favorable for the development of the Yuedong upwelling, but unfavorable for the upwelling in the Taiwan Bank (A further explanation is given later). The longer duration of the prevailing upwelling-favorable wind causes a stronger Yuedong upwelling on 8 July than on 26 June (Figure 6e versus 7e). The surface salinity field in Case C differs remarkably from that in Case A (Figure 7f). The river plume axis is directed northeastward between the two upwelling regions rather than offshore as in Case A. The surface currents are reduced without the baroclinic effect, so the plume water distributed in the northeastern SCS is reduced. From 26 June to 8 July, the upwelling-favorable wind drives the river plume 200 km further northeastward off the Yuedong upwelling region in barotropic Case C.

3.3. Freshwater Transport and Fluxes
The river plume shows spatiotemporal variations modulated by varying upwelling intensities, in response to different wind forcing and the inclusion of the baroclinic effect. According to *Choi and Wilkin* [2006] and *Li*
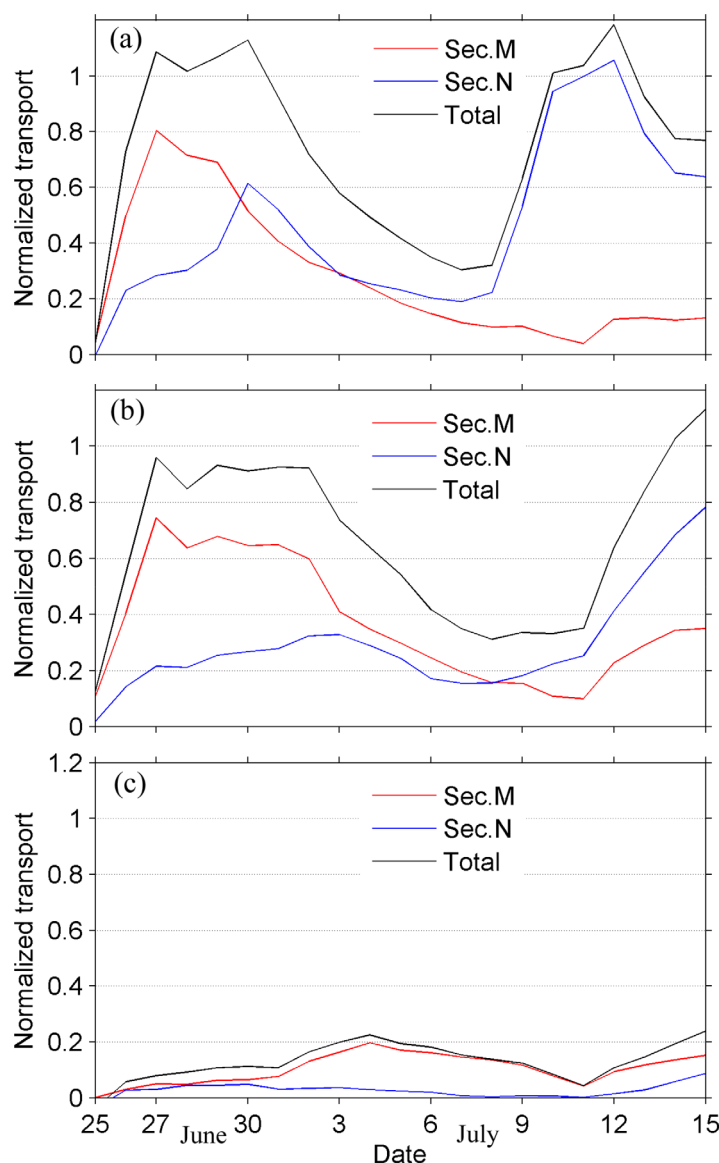
Figure 8. Time series of normalized freshwater transport for (a) Case A, (b) Case B, and (c) Case C. Red and blue lines represent freshwater transport through Sections M and N, respectively. Black line represents the total freshwater transport, summing up that in Sections M and N. Locations of Sections M and N are shown in Figure 7a.

and Rong [2012], the alongshore and offshore freshwater transports associated with the river plume in Sections M and N (Figure 7a) are estimated by

$$Q_f = \int\int v\left(1 - \frac{S}{S_0}\right)dA, \quad (1)$$

where v is the horizontal velocity normal to the section, S is the water salinity, $S_0 = 34.13$ is the ambient seawater salinity. (We select the average in situ salinity in the upper 100 m of the water column at Station C7, far from the river plume.) As the plume water is in the surface layer, the variable $v(1 - S/S_0)$ is vertically integrated in a water column shallower than 100 m and is horizontally integrated along the section. Time series of freshwater transport normalized by river discharge, Q_f/Q_0 in Sections M and N for the three cases, are given in Figure 8.

In the initial stage of the periodic upwelling-favorable wind, the river plume is primarily transported alongshore across Section M in Case A (Figure 8a). The freshwater transport alongshore reaches a maximum value of $0.8Q_0$ on 27 June. The Yuedong upwelling then develops continually, and the alongshore conduit between the two upwelling regions is gradually shut down. Accordingly, the alongshore freshwater transport gradually declines, reaching

$0.1Q_0$ after 9 July. The burst of upwelling-favorable wind also induces an increase in offshore freshwater transport, which shows a peak value of $0.6Q_0$ on 30 June, and decreases thereafter, because the upwelling-favorable wind is reduced. The following lasting upwelling-favorable wind induces the transport of large amounts of freshwater offshore from 8 to 15 July. The main freshwater transport switches from alongshore during the initial stage of the upwelling to offshore when the upwelling is strong. The total freshwater transport in the northeastern SCS fluctuates in June and July, and the Q_0 value peaks from 27 to 30 June and from 10 to 13 July. Overall, 74% of the Pearl River discharge is transported to the northeastern SCS from 25 June to 15 July, during which offshore freshwater transport occupies 63% and the rest is alongshore.

Compared with Case A, the freshwater transport through Section M increases, and the total freshwater transport is reduced in Case B (Figure 8b). The weaker upwelling-favorable wind results in a weaker surface Ekman current and a lower intensity of the Yuedong upwelling. As a result, less freshwater ($0.66Q_0$) is transported to the northeastern SCS, 56% of which is transported through Section M between the two upwelling

regions. The ratio is greater than that in Case A, because of the reduced offshore Ekman transport and Yue-dong upwelling area.

In barotropic Case C, the total freshwater transport is reduced by 1 order of magnitude ($0.13Q_0$) and primarily crosses Section M (Figure 8c). The wind drift and barotropic coastal geostrophic current can drive only small amounts of freshwater eastward to the northeastern SCS. Without the baroclinic effect, the coastal current at the upwelling front weakens, which is unfavorable for eastward freshwater transport in the northeastern SCS.

To further investigate the dynamic effects on the freshwater transport surrounding the upwelling regions with different forcing agents, the depth-integrated freshwater flux per unit width is computed and decomposed into three terms following *Uncles and Lewis* [2001] and *Tarya et al.* [2015]:

$$\langle F_f \rangle = \langle Q \rangle \langle \bar{\gamma} \rangle + \langle h\overline{u'\gamma'} \rangle + \langle \tilde{Q}\tilde{\gamma} \rangle, \tag{2}$$

where the angle brackets denote the tidal cycle average (25 h in this study), the overbars denote the depth-averaged values, h is the water depth, u is the horizontal velocity, $Q = h\bar{u}$ is the water flux per unit width, $\gamma = 1 - S/S_0$ is the freshwater fraction, the primes denote the differences between the variables and their depth-averaged values, and the tildes denote fluctuations of depth-averaged variables in a tidal cycle. On the right-hand side, the first term is the advective freshwater flux by depth-averaged and tidally averaged flow, the second term is the vertical shear freshwater flux caused by depth variations of horizontal velocity and salinity, and the third term is the contribution from tidal pumping. The contribution of the tidal pumping effect to the total freshwater flux is negligible (<3%), so it is not shown here.

The freshwater fluxes in Cases A to C on 26 June are shown in Figure 9. In Cases A and B, the freshwater fluxes are mainly concentrated between the two upwelling regions (Figures 9a and 9d). Most of them are northeastward, and some are transported eastward. Advection is the dominant contributor to the
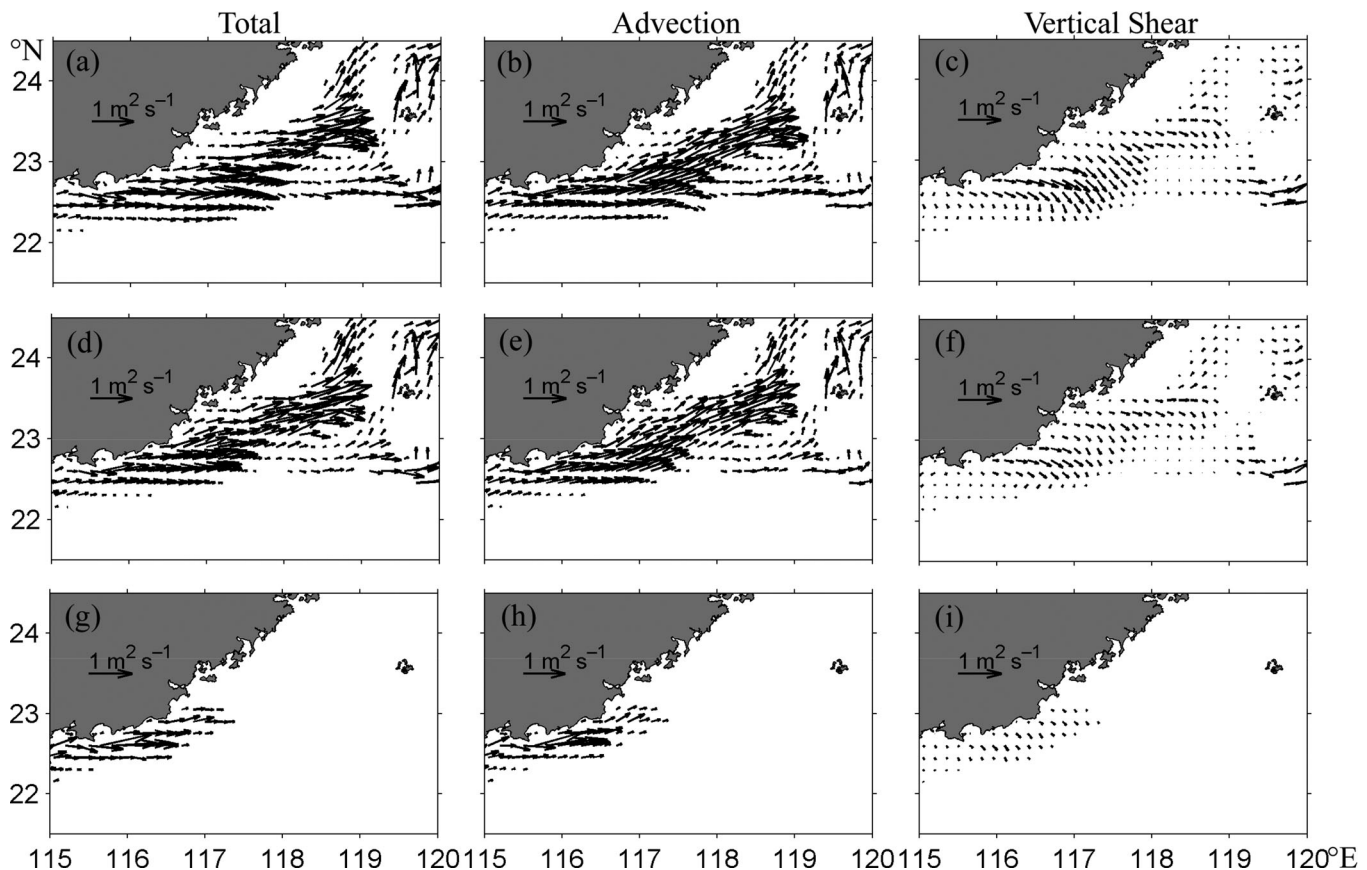
Figure 9. Depth-integrated freshwater fluxes (m^2 s^{-1}) on 26 June 2011 for (a–c) Case A, (d–f) Case B, and (g–i) Case C. The left column shows the total flux, the middle column shows the flux due to advection, and the right column shows the flux due to vertical shear. The regions with salinity higher than 33.5 are blanked.
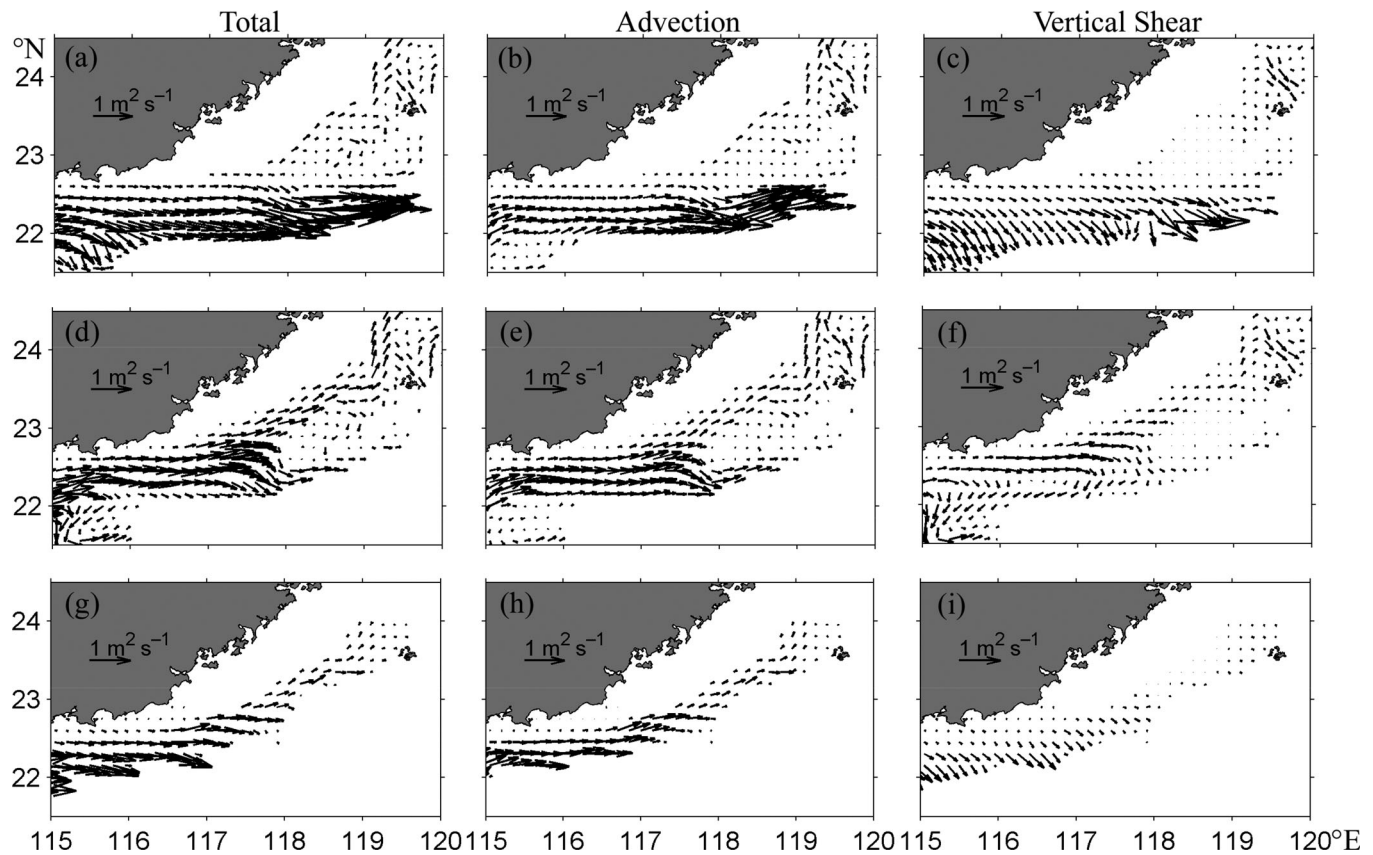
Figure 10. Same as Figure 9, but for 8 July 2011.

freshwater fluxes, and the distribution patterns are similar to those of the total freshwater fluxes (Figures 9b and 9e). Vertical shear plays a minor role in the freshwater fluxes (Figures 9c and 9f). In Case C, the plume water is confined near the coast west of 117°E and is primarily driven by the advection effect (Figures 9g–9i). Overall, the Pearl River freshwater transport in the northeastern SCS is dominated by advective transport for Cases A–C, and the vertical shear plays a secondary role.

The freshwater fluxes on 8 July are shown in Figure 10 under the condition that upwelling-favorable wind forces on the sea surface for 10–12 days. In Case A, large freshwater flux is transported eastward to the outer-shelf 200 km offshore, and the advection overwhelms the vertical shear in its contribution to the freshwater flux (Figures 10a–10c). More freshwater fluxes are transported through the two upwelling regions in Case B than in Case A (Figures 10d–10f). In Case C, the freshwater flux largely decreases, and the dominant advective transport brings it alongshore off the Yuedong upwelling (Figures 10g–10i). Although the upwelling strength and forcing vary over time in all of the cases, the advection component always dominates the total freshwater flux. The freshwater fluxes by the vertical shear are primarily directed offshore.

4. Discussion

4.1. Mechanisms for Offshore Freshwater Transport

The dynamics of the river plume surrounding the upwelling regions can be further analyzed via the momentum equation. Omitting the small vertical advection, the momentum equation in the cross-shore direction is given by

$$
\underbrace{\frac{\partial V}{\partial t}}_{ACCEL} = -\underbrace{(U\frac{\partial V}{\partial x} + V\frac{\partial V}{\partial y})}_{HADV} - \underbrace{fU}_{COR} - \underbrace{\frac{1}{\rho}\frac{\partial P}{\partial y}}_{PGF} + \underbrace{\frac{\partial}{\partial x}(A_h\frac{\partial V}{\partial x}) + \frac{\partial}{\partial y}(A_h\frac{\partial V}{\partial y})}_{HVISC} + \underbrace{\frac{\partial}{\partial z}(A_z\frac{\partial V}{\partial z})}_{VVISC}, \tag{3}
$$

where U and V are the along and cross-shore velocities, f is the Coriolis parameter, ρ is the sea water density, P is the pressure, A_h is the diffusivity coefficient, and A_z is the eddy viscosity. The term on the left-hand side
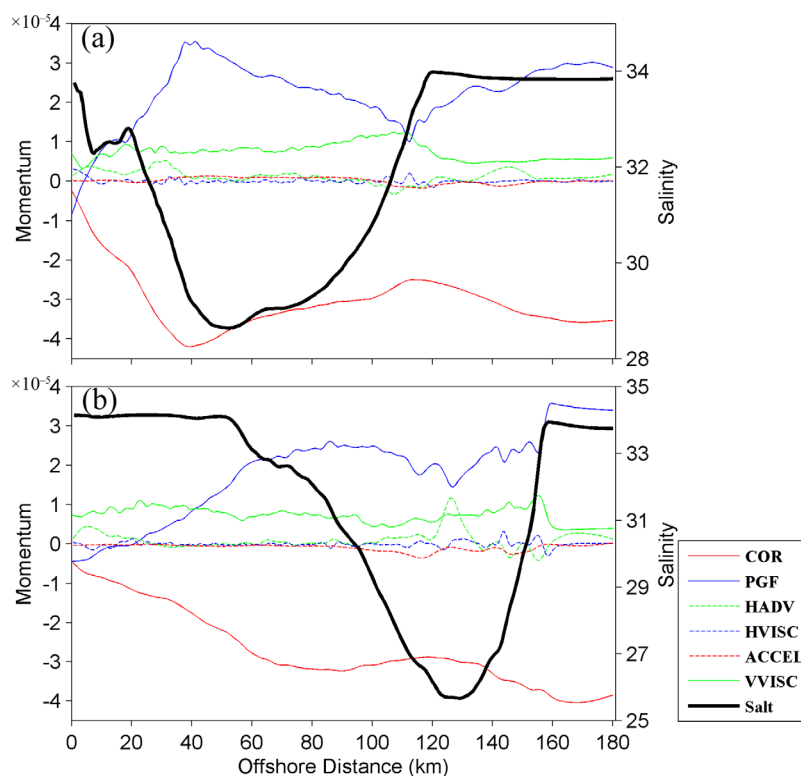
Figure 11. Surface momentums (m s^{-2}) and salinity (psu, black solid line) in Section P on (a) 26 June and (b) 8 July 2011, in which COR represents the Coriolis force, PGF the pressure gradient, HADV the horizontal advection, HVISC the horizontal diffusion, ACCEL the acceleration, VVISC the vertical diffusion. Positive values direct onshore. Location of Section P and directions of alongshore and cross-shore velocities are shown in Figure 7a.

is the local acceleration (ACCEL), and the terms on the right-hand side are the horizontal advection (HADV), Coriolis force (COR), pressure gradient force (PGF), horizontal diffusion (HVISC), and vertical diffusion (VVISC), respectively.

The daily mean surface momentums and the surface salinity in cross-shore Section P (location shown in Figure 7a) are displayed in Figure 11. The momentum balance is dominated by a geostrophic balance on both 26 June and 8 July. The average Rossby number R_o equals 0.04 and the average Ekman number E_k is smaller than 0.25 in the plume area, illustrating that the advection and friction terms are relatively small in the momentum balance. The PGF shows a peak value of 3.5×10^{-5} m s^{-2} 40 km offshore on 26 June (Figure 11a). When the upwelling is in its initial stage, low-salinity water (<32 psu) is distributed 25–110 km offshore, corresponding to the coastal area with a PGF greater than 2×10^{-5} m s^{-2}. This is analogous to a geostrophic current faster than 0.37 m s^{-1}. The VVISC is approximately 1×10^{-5} m s^{-2} in the section, corresponding to a surface alongshore Ekman current of 0.18 m s^{-1}. When the upwelling is fully developed on 8 July, the zone with a relatively high PGF moves offshore (Figure 11b), and low-salinity water is accordingly shifted to 80–155 km offshore. The plume axis is pushed from 50 km offshore on 26 June to 130 km offshore on 8 July. The coastal region is occupied by upwelled subsurface high-salinity water and the PGF there becomes relatively low. It is suggested that the development of the Yuedong upwelling causes the coastal zone with a high PGF (fast geostrophic current) to move offshore, where it preferentially diverts the Pearl River plume offshore.

The movement of the river plume associated with the development of the upwelling is further analyzed. Time series of salinity, temperature, and PGF in Section P in Case A are displayed in Figure 12. The plume shows a zigzag pattern, in keeping with the upwelling and periodic upwelling-favorable winds (Figure 12a). The plume axis moves offshore from 24 to 27 June and onshore in the following 6 days. Large amounts of plume water are driven offshore from 3 to 10 July, reaching as far as 160 km offshore. The speed of the offshore current reaches 0.19 m s^{-1} (as computed from the slope of the low-salinity water in Figure 12a),
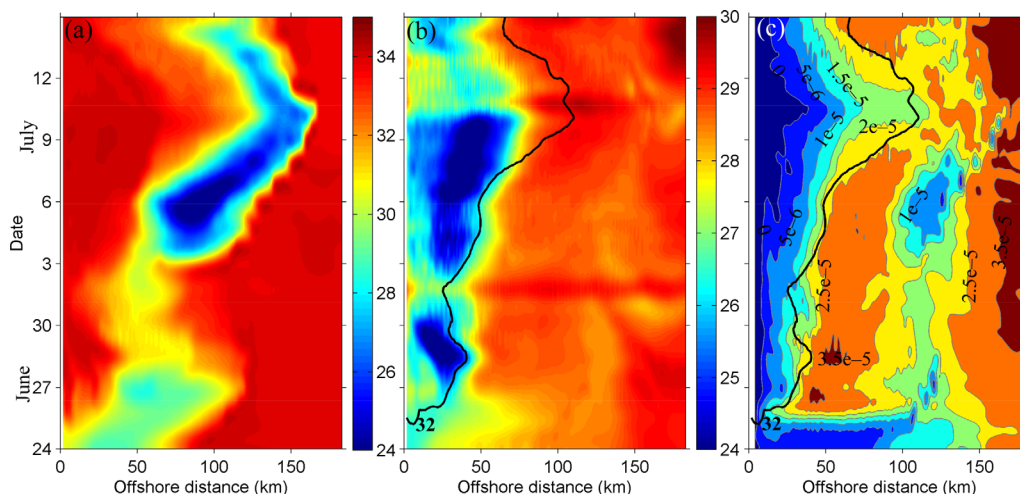
Figure 12. Hovmöller diagrams of (a) surface salinity (psu), (b) SST (°C), and (c) surface PGF (m s^{-2}) in Section P for Case A. Black lines are 32 psu isohaline in Figures 12b and 12c denoting time series of onshore boundary of plume water. Data are low-pass filtered with a 33 h filter to remove tidal oscillations.

which is induced by the offshore Ekman drift and the upwelling circulation. However, the plume's offshore movement speed is reduced to approximately 0.06 m s^{-1} in barotropic Case C, and the plume water reaches a maximum of 120 km offshore (not shown). The river plume arriving in the northeastern SCS retains a salinity between 24 and 31 psu on the axis, and its width varies from 20 to 70 km. The variation of the Yuedong upwelling intensity in Section P is shown in Figure 12b. Relatively cold water is present from 24 June to 15 July. An upwelling develops from the coastal region on 24 June to 50 km offshore on 27 June. It then relaxes before continually intensifying from 3 to 10 July due to the burst of upwelling-favorable wind. The relatively cold water can extend to 80 km offshore, and the temperature drops at least 5°C in the upwelling core. The plume trajectory is closely related to the variation in the upwelling intensity. The plume's near-shore boundary (32 isohaline) follows the Yuedong upwelling front before 8 July. It is then pushed further offshore, but still keeps pace with the upwelling variation. To explain the river plume's off-shore movement, time series of the surface PGF are displayed in Figure 12c. The coastal upwelling region is occupied by a relatively low PGF. As the upwelling develops, the low PGF ($<1.5 \times 10^{-5}$ m s^{-2}) covers from an inshore area on 25 June to a far offshore area on 11 July. Consequently, the relatively high PGF zone is squeezed offshore as a result of intensive upwelling. The relatively high PGF zone generates a fast geo-strophic current, and its offshore movement leads to an offshore shift of the plume water. The plume's near-shore boundary changes over time but is confined within the PGF zone in the range of 1.5×10^{-5} to 2.5×10^{-5} m s^{-2} off the upwelling region. The plume trajectory follows the coastal zone with a relatively high PGF, which is closely related to the strength of the Yuedong upwelling.

To illustrate why the zone with a relatively high PGF moves offshore as the upwelling develops, we plot the spatial distributions of sea level (Figure 13a) and surface temperature (Figure 13b) on 26 June and 8 July. In the upwelling's initial stage, the coastal region is occupied by the relatively high horizontal gra-dient of sea level (contours in Figure 13a). Currents preferentially travel along the near-shore isobars, bringing the river plume through the two separate upwelling regions. When the upwelling-favorable wind blows for 10–12 days, a strong upwelling develops. Ekman transport drives the surface sea water offshore, which shifts the zone with a relatively high barotropic PGF offshore (shading in Figure 13a); it may encircle the upwelling in the Taiwan Bank. The channel between the two upwelling regions with a northeastward barotropic geostrophic current is gradually shut down. In addition, the Yuedong upwelling front moves offshore from 26 June to 8 July (Figure 13b). Accordingly, the zone with a relatively high bar-oclinic PGF also moves offshore. As the Yuedong upwelling develops, the offshore shift of the relatively high horizontal gradient of sea level and the upwelling front causes the zone with a relatively high PGF to spread offshore. When the Yuedong upwelling is fully developed, the isobars are directed eastward, and the Pearl River plume that arrives at the west of the Yuedong upwelling is brought eastward to the east of the Taiwan Bank.
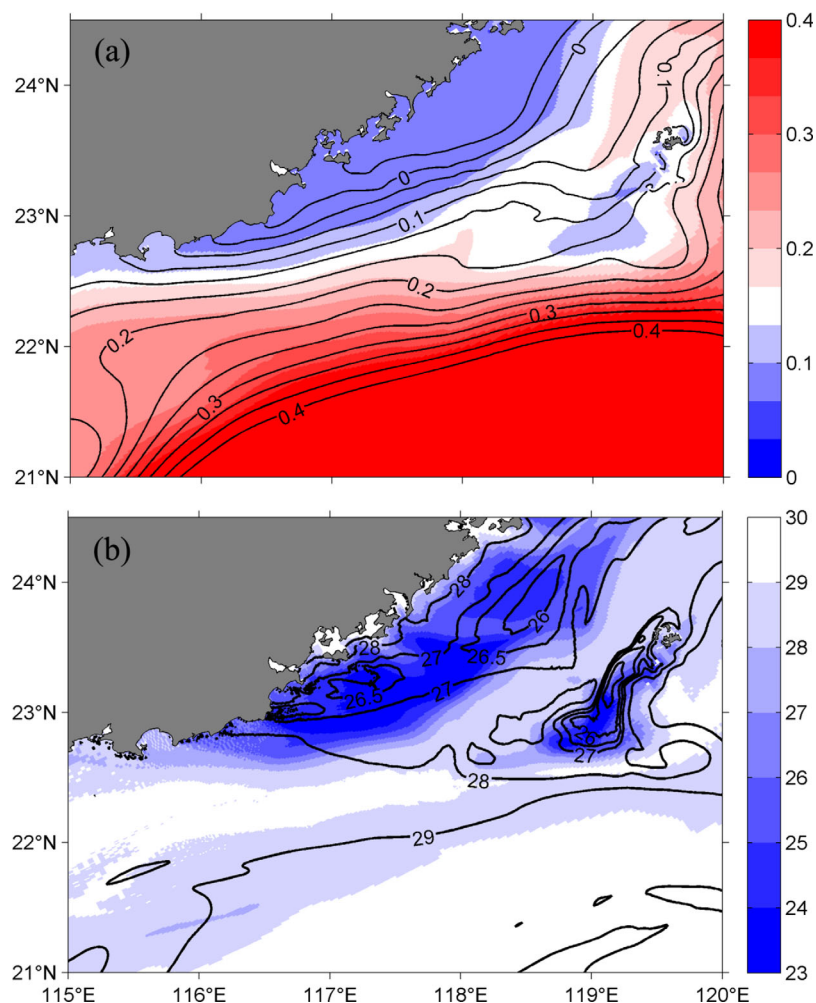
Figure 13. (a) The sea level (m) on 26 June (black contours), and 8 July 2011 (color shading) for Case A. The contours and shading interval are 0.33 m. Sea level data are low-pass filtered with a 33 h filter. (b) The surface temperature (°C) on 26 June (black contours), and 8 July 2011 (blue shading), also the same as Figures 6a and 7a.

4.2. Forcing Agents on Upwelling and River Plume

The northeastern SCS's hydrodynamics are complicated. Plume water, upwelled water, subsurface water, upper warm water, and mixed water coexist there during summer [*Hu et al.*, 2011]. The different water masses coexist in the northeastern SCS, forming complicated frontal structures [*Li et al.*, 2000]. The wind forcing and interaction between currents and topography act upon the Yuedong upwelling, and the tides are responsible for the upwelling in the Taiwan Bank [*Wang et al.*, 2014; *Jiang et al.*, 2011]. The mechanisms for the two upwellings were also summarized in a review study by *Hu and Wang* [2016], who noted that the alongshore wind was the primary factor in the generation of the Yuedong upwelling, whereas both tidal mixing and the interaction between the bottom current and the topography contributed to forming the upwelling in the Taiwan Bank. As the mechanisms of the two upwellings have different influencing factors, their variations are independent of each other.

The upwelling interacts with the river plume, and both should be considered when studying the dynamics in response to the varied forcing agents in the northeastern SCS. The dynamics of the Pearl River plume out of the estuary are mainly determined by internal stress and wind [*Pan and Gu*, 2016]. The development of the upwelling can influence the plume's trajectory, dynamics, and freshwater transport. The upwelling process induces the patched structure of the Pearl River plume in the northern SCS [*Chen et al.*, 2016], and the upwelling's cross-shelf circulation is also enhanced by the plume in the upper water column [*Gan et al.*, 2009b].

The upwelling, wind, and baroclinic effects determine the dynamics, pathway, and fate of the Pearl River plume. The wind varies in strength, direction, and duration during summer, which causes the strength of the Yuedong upwelling to vary over time. The strength of the Yuedong upwelling alters the trajectory of the river plume, and the wind also plays an important role in dispersing the river plume over the shelf. A surface Ekman effect acts upon both the upwelling and river plume. The dynamics of the plume adjacent to the upwelling are modulated by the upwelling circulation and the related stratification. In Case C, the pressure gradient induced by variations in density is excluded, so the vertical pressure disturbance vanishes, resulting in a low Brunt-Väisälä frequency. The reduced stratification facilitates the upwelling of the subsurface water to the surface in the Taiwan Bank. However, the mechanism differs for the Yuedong upwelling. The Joint Effect of Baroclinicity and Relief (JEBAR) contributes to the onshore transport of cold subsurface water at the widened shelf in the northeastern SCS, although it is relatively lesser than the effects of Ekman transport and Ekman pumping [*Wang et al.*, 2014]. The Yuedong upwelling on 8 July is thus diminished without the baroclinic effect in Case C. When the Yuedong upwelling is strong, a baroclinic jet forms at its front, which determines the plume dynamics entrained in the jet [*Chen et al.,* 2017]. Upwelling-induced baroclinic jet facilitates the eastward transport of Pearl River plume, and baroclinic effect is crucial to the amount of plume water reaching the Taiwan Strait.

The effects of the tides and the widened shelf may also influence the two upwellings and the surrounding plume dynamics. Although the effect of tidal pumping on the river plume is weak in the northeastern SCS, the tides are important in triggering the upwelling in the Taiwan Bank. Accordingly, the freshwater transport and plume fate can be changed during spring-neap tidal circles. The strong shoreward bottom current driven by the westward PGF occurs at the head of the widened shelf, thus intensifying the Yuedong upwelling [*Gan et al.*, 2009a]. Meanwhile, the surface coastal current veers offshore there, which steers the trajectory of the eastward Pearl River plume [*Gan et al.*, 2009b; *Shu et al.*, 2014]. Idealized numerical modeling results given by *Xing and Davies* [2002] also show that the topographically steered current drives the surface plume water offshore in the widened shelf region.

Wind varies over time and causes differences in freshwater transport in the northeastern SCS and changes the partition ratio of the alongshore freshwater transport through the two upwelling regions related to the upwelling intensity. The choice of the benchmark sea water salinity, S_0 in equation (1), is subjective, which may introduce some absolute errors into the freshwater transport computation. However, the trends of the time evolution of freshwater transport in response to the varied upwelling and forcing agents are reasonable. A constant reference salinity is commonly chosen to estimate the freshwater transport [e.g., *Isobe et al.*, 2002; *Choi and Wilkin*, 2006; *Li and Rong*, 2012]. Although advection is the dominant contributor to the total freshwater flux in the northeastern SCS, it should be noted that the relative contributions of advection, vertical shear, and tidal pumping can vary as the Pearl River plume travels from its origin to its destination.

4.3. Entrainment of Plume Water by Eddies

Mesoscale eddies are active in the SCS. Each year, 32.8 ± 3.4 eddies form with radii between 46.5 and 223.5 km, but 70% have a radius smaller than 100 km [*Xiu et al.*, 2010]. Cyclonic and anticyclonic eddies from large scale to submesoscale propagate westward and modulate the northern SCS's hydrography and circulation [*Wu and Chiang*, 2007; *Li et al.*, 2011]. The entrainment of plume water by eddies in tandem with the fully developed Yuedong upwelling is exemplified in Figure 14. The Yuedong upwelling and upwelling in the Taiwan Bank are characterized by relatively low SST and high turbidity. The turbid plume water with a relatively high SST is transported eastward, when the Yuedong upwelling is fully developed. This offshore plume water encounters eddies over the outer-shelf, and is transported to 250 km offshore by the cyclonic and anticyclonic eddies. The cross-shore transport of plume water provides nutrients to the oligotrophic open sea, which enhances the biological productivity there. It should be noted that this scenario only occurs under the conditions of fully developed Yuedong upwelling and intrusion of active eddies to the shelf region. Interaction of the buoyant plume with eddies can also be found in the northern Gulf of Mexico region, where the Mississippi River plume is brought by eastward wind-driven currents toward the shelf break and is further entrained into the eddies [*Schiller et al.*, 2011]. The Pearl River plume entrained by eddies in the northern SCS needs to be further explored.

Based on the MODIS turbidity image, hydrographic measurement, and SLA data, we estimate the freshwater transport entrained by the eddies to the open ocean. Assuming that plume water with a salinity of 32 psu
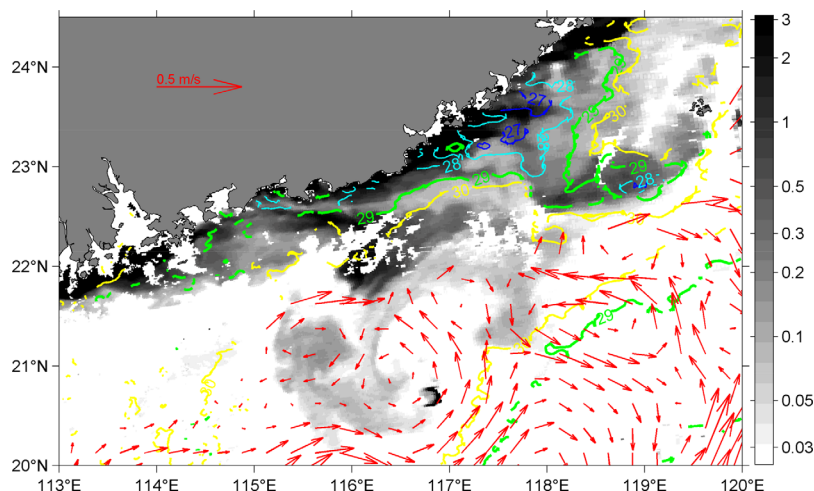
Figure 14. Turbidity (NTU; black shading) and SST (°C; contours) from the MODIS satellite images on 22 August 2014. The corresponding geostrophic currents derived from the SLA (red vectors), where the water depth shallower than 100 m is blanked.

and a thickness of 20 m is entrained into the eddies at a width of 150 km (i.e., the sum of the width of the cyclonic and anticyclonic eddies in Figure 14) and a speed of 0.1 m s^{-1} (i.e., the geostrophic current derived from the SLA), the freshwater transport is estimated to be approximately 1.87 $\times$ 10^4 m^3 s^{-1} (viz., [1–32/34.13] $\times$ 150 km $\times$ 20 m $\times$ 0.1 m s^{-1}). It reaches the magnitude of the Pearl River discharge during summer, which means that most of the freshwater is entrained into the eddies. The turbidity image also demonstrates that the eastward transport of the plume water is finally trapped in the eddies. If the fully developed upwelling and active eddies over the outer-shelf occur on a synoptic time scale of 7 days, the eddy-induced offshore removal of freshwater is approximately 1.13 $\times$ 10^{10} ton.

5. Conclusions

A combination of in situ observations, remote sensing, and numerical modeling is used to study the Pearl River plume dynamics and freshwater transport as responses to the complex upwelling systems in the northeastern SCS. Observations show that the plume axis passes through the two separate upwelling regions and that some plume water leaks to the outer-shelf, when the Yuedong upwelling is at moderate strength. When the Yuedong upwelling is fully developed in tandem with the upwelling in the Taiwan Bank, most of the plume water is transported eastward until it reaches 200 km offshore. The numerical modeling results are verified by the observations, and the model reproduces the upwelling phenomena and the river plume's spatial distribution.

Numerical modeling experiments are carried out to examine the wind strength and baroclinic effects on the two upwellings, the plume dispersal, and the freshwater transport. In the normal run (Case A), the plume water is primarily transported alongshore, sandwiched between the two separate upwelling regions in the initial stage of the Yuedong upwelling. As the Yuedong upwelling develops, the offshore freshwater transport gradually overwhelms its alongshore counterpart. In Case B, the wind strength is reduced to one tenth of that in Case A. The Yuedong upwelling is weaker, and more plume water travels alongshore, passing through the two upwelling regions. In Case C without a baroclinic effect, the Yuedong upwelling weakens and the upwelling in the Taiwan Bank intensifies. The currents at the Yuedong upwelling front slow down. As a result, a small amount of the Pearl River plume water is transported to the northeastern SCS, located between the two upwelling regions. Advection is the dominant contributor to the total freshwater transport flux in all cases. Vertical shear plays a secondary role in the freshwater flux, but tidal pumping is negligible.

Dynamic analysis reveals that geostrophic balance dominates in the coastal upwelling and plume areas. When the Yuedong upwelling is in its initial stage, a zone with relatively high PGF is located near the shore, and the river plume travels northeastward along the Yuedong upwelling front. As the upwelling-favorable wind blows for 10–12 days, the Yuedong upwelling is strong. The relatively high horizontal gradient of sea

level moves offshore, because of the offshore Ekman transport. Meanwhile, upwelling circulation shifts the upwelling front offshore. These two effects induce offshore movement of the zone with a relatively high PGF. In that case, the plume water travels preferentially along the fast geostrophic current far from the coast until east of the Taiwan Bank, when the Yuedong upwelling is fully developed. When plume water is transported offshore by the fully developed Yuedong upwelling, sometimes the active eddies over the outer-shelf in the northern SCS may bring it further to the open sea, which is significant to the cross-shore transport of river-borne terrigenous materials, such as sediments, nutrients, and pollutants.

References

Bai, Y., et al. (2015), Intrusion of the Pearl River plume into the main channel of the Taiwan Strait in summer, *J. Sea Res.*, *95*, 1–15.

Cai, S. Z., R. S. Wu, and J. D. Xu (2011), Characteristics of upwelling in eastern Guangdong and southern Fujian coastal waters during 2006 summer [in Chinese with English abstract], *J. Oceanogr. Taiwan Strait*, *30*, 489–497.

Chen, S. N. (2014), Enhancement of alongshore freshwater transport in surface-advected river plumes by tides, *J. Phys. Oceanogr.*, *44*, 2951–2971.

Chen, Z., X.-H. Yan, and Y. Jiang (2014), Coastal cape and canyon effects on wind-driven upwelling in northern Taiwan Strait, *J. Geophys. Res. Oceans*, *119*, 4605–4625, doi:10.1002/2014JC009831.

Chen, Z., J. Pan, and Y. Jiang (2016), Role of pulsed winds on detachment of low salinity water from the Pearl River Plume: Upwelling and mixing processes, *J. Geophys. Res. Oceans*, *121*, 2769–2788, doi:10.1002/2015JC011337.

Chen, Z., J. Pan, Y. Jiang, and H. Lin (2017), Far-reaching transport of Pearl River plume water by upwelling jet in the northeastern South China Sea, *J. Marine Syst.*, *173*, 60–69.

Choi, B.-J., and J. L. Wilkin (2006), The effect of wind on the dispersal of the Hudson River plume, *J. Phys. Oceanogr.*, *37*, 1878–1897.

Egbert, G. D., and S. Y. Erofeeva (2002), Efficient inverse modeling of barotropic ocean tides, *J. Atmos. Oceanic Technol.*, *19*, 183–204.

Fong, D. A., and W. R. Geyer (2001), Response of a river plume during an upwelling favorable wind event, *J. Geophys. Res.*, *106*(C1), 1067–1084.

Fong, D. A., and W. R. Geyer (2002), The alongshore transport of freshwater in a surface-trapped river plume, *J. Phys. Oceanogr.*, *32*, 957–972.

Gan, J., A. Cheung, X. Guo, and L. Li (2009a), Intensified upwelling over a widened shelf in the northeastern South China Sea, *J. Geophys. Res.*, *114*, C09019, doi:10.1029/2007JC004660.

Gan, J., L. Li, D. X. Wang, and X. G. Guo (2009b), Interaction of a river plume with coastal upwelling in the northeastern South China Sea, *Cont. Shelf Res.*, *29*, 728–740.

García-Berdeal, I., B. M. Hickey, and M. Kawase (2002), Influence of wind stress and ambient flow on high discharge river plume, *J. Geophys. Res.*, *107*(C9), 3130, doi:10.1029/2001JC000932.

Geyer, W. R. (1995), Tide-induced mixing in the Amazon frontal zone, *J. Geophys. Res.*, *100*(C2), 2341–2353, doi:10.1029/94JC02543.

Hong, H.-S., et al. (2009), Three-dimensional structure of a low salinity tongue in the southern Taiwan Strait observed in the summer of 2005, *Acta Oceanol. Sin.*, *28*, 1–7.

Hu, J., and X. H. Wang (2016), Progress on upwelling studies in the China seas, *Rev. Geophys.*, *54*, 653–673, doi:10.1002/2015RG000505.

Hu, J. Y., H. X. Liang, and X. B. Zhang (1999), Distributional features of temperature and salinity in southern Taiwan Strait and its adjacent sea areas in late summer, 1994, *Acta Oceanol. Sin.*, *18*, 237–246.

Hu, J. Y., H. Kawamura, H. S. Hong, and W. R. Pan (2003), A review of research on the upwelling in the Taiwan Strait, *Bull. Mar. Sci.*, *73*(3), 605–628.

Hu, J. Y., H. Kawamura, C. Y. Li, H. S. Hong, and Y. W. Jiang (2010), Review on current and seawater volume transport through the Taiwan Strait, *J. Oceanogr.*, *66*, 591–610.

Hu, J. Y., et al. (2011), Variable temperature, salinity and water mass structures in the southwestern Taiwan Strait in summer, *Cont. Shelf Res.*, *31*, S13–S23.

Huang, Y. C., Y. Li, H. Shao, and Y. H. Li (2008), Seasonal variations of sea surface temperature, chlorophyll a and turbidity in Beibu Gulf, MODIS imagery study, *J. Xiamen Univ.*, *47*(6), 856–863.

Isobe, A., M. Ando, T. Watanabe, T. Senjyu, S. Sugihara, and A. Manda (2002), Freshwater and temperature transports through the Tsushima-Korea Straits, *J. Geophys. Res.*, *107*(C7), 3065, doi:10.1029/2000JC000702.

Jan, S., J. Wang, C. S. Chern, and S. Y. Chao (2002), Seasonal variation of the circulation in the Taiwan Strait, *J. Mar. Syst.*, *35*, 249–268.

Jiang, Y. W., F. Chai, Z. W. Wan, X. Zhang, and H. S. Hong (2011), Characteristics and mechanisms of the upwelling in the southern Taiwan Strait: A three-dimensional numerical model study, *J. Oceanogr.*, *67*, 699–708.

Kim, C.-S., Y.-K. Cho, G.-H. Seo, B.-J. Choi, K. T. Jung, and B.-G. Lee (2014), Interannual variation of freshwater transport and its causes in the Korea Strait: A modeling study, *J. Mar. Syst.*, *132*, 66–74.

Large, W. G., J. C. McWilliams, S. C. Doney (1994), Oceanic vertical mixing: A review and a model with a nonlocal boundary layer parameterization, *Rev. Geophys.*, *32*, 363–403, doi:10.1029/94RG01872.

Li, J. X., R. Zhang, and B. G. Jin (2011), Eddy characteristics in the northern South China Sea as inferred from Lagrangian drifter data, *Ocean Sci.*, *7*, 661–669.

Li, L., X. G. Guo, and R. S. Wu (2000), Oceanic fronts in southern Taiwan Strait [in Chinese with English abstract], *J. Oceanogr. Taiwan Strait*, *19*, 147–156.

Li, M., and Z. Rong (2012), Effects of tides on freshwater and volume transports in the Changjiang River plume, *J. Geophys. Res.*, *117*, C06027, doi:10.1029/2011JC007716.

Lin, X. Y., X.-H. Yan, Y. W. Jiang, and Z. C. Zhang (2016), Performance assessment for an operational ocean model of the Taiwan Strait, *Ocean Modell.*, *102*, 27–44.

Ou, S. Y., H. Zhang, and D. X. Wang (2009), Dynamics of the buoyant plume off the Pearl River Estuary in summer, *Environ. Fluid Mech.*, *9*, 471–492.

Pan, J., and Y. Gu (2016), Cruise observation and numerical modeling of turbulent mixing in the Pearl River estuary in summer, *Cont. Shelf Res.*, *120*, 122–138.

Pan, J., Y. Gu, and D. Wang (2014), Observations and numerical modeling of the Pearl River plume in summer season, *J. Geophys. Res. Oceans*, *119*, 2480–2500, doi:10.1002/2013JC009042.

Schiller, R. V., V. H. Kourafalou, P. Hogan, and N. D. Walker (2011), The dynamics of the Mississippi River plume: Impact of topography, wind and offshore forcing on the fate of plume waters, *J. Geophys. Res.*, 116, C06029, doi:10.1029/2010JC006883.

Shchepetkin, A. F., and J. C. McWilliams (2005), The regional ocean modeling system: A split-explicit, free-surface, topography-following coordinates ocean model, *Ocean Modell.*, 9, 347–404.

Shu, Y. Q., D. X. Wang, J. Zhu, and S. Q. Peng (2011), The 4-D structure of upwelling and Pearl River plume in the northern South China Sea during summer 2008 revealed by a data assimilation model, *Ocean Modell.*, 36, 228–241.

Shu, Y. Q., J. Chen, J. L. Yao, J. Y. Pan, W. W. Wang, H. B. Mao, and D. X. Wang (2014), Effects of the Pearl River plume on the vertical structure of coastal currents in the Northern South China Sea during summer 2008, *Ocean Dyn.*, 64, 1743–1752.

Su, J. (2004), Overview of the South China Sea circulation and its influence on the coastal physical oceanography outside the Pearl River Estuary, *Cont. Shelf Res.*, 24, 1745–1760.

Tang, D. L., D. R. Kester, I. Ni, H. Kawamura, H. S. Hong (2002), Upwelling in the Taiwan Strait during the summer monsoon detected by satellite and shipboard measurements, *Remote Sens. Environ.*, 83(3), 457–471.

Tarya, A., M. van der Vegt, and A. J. F. Hoitink (2015), Wind forcing controls on river plume spreading on a tropical continental shelf, *J. Geophys. Res. Oceans*, 120, 16–35, doi:10.1002/2014JC010456.

Uncles, R. J., and R. E. Lewis (2001), The transport of fresh water from river to coastal zone through a temperate estuary, *J. Sea Res.*, 46(2), 161–175.

Wang, D., W. Zhuang, S.-P. Xie, J. Hu, Y. Shu, and R. Wu (2012), Coastal upwelling in summer 2000 in the northeastern South China Sea, *J. Geophys. Res.*, 117, C04009, doi:10.1029/2011JC007465.

Wang, D., et al. (2014), Relative contributions of local wind and topography to the coastal upwelling intensity in the northern South China Sea, *J. Geophys. Res. Oceans*, 119, 2550–2567, doi:10.1002/2013JC009172.

Wong, L. A., J. C. Chen, H. Xue, L. X. Dong, W. B. Guan, and J. L. Su (2003), A model study of the circulation in the Pearl River Estuary (PRE) and its adjacent coastal waters: 2. Sensitivity experiments, *J. Geophys. Res.*, 108(C5), 3157, doi:10.1029/2002JC001452.

Wu, C.-R., and T.-L. Chiang (2007), Mesoscale eddies in the northern South China Sea, *Deep Sea Res., Part II*, 54, 1575–1588.

Wu, H., J. Zhu, J. Shen, and H. Wang (2011), Tidal modulation on the Changjiang River plume in summer, *J. Geophys. Res.*, 116, C08017, doi: 10.1029/2011JC007209.

Xing, J. X., and A. M. Davies (2002), Influence of topographic features and along shelf flow upon the Ebro plume, *Cont. Shelf Res.*, 22, 199–227.

Xiu, P., F. Chai, L. Shi, H. Xue, and Y. Chao (2010), A census of eddy activities in the South China Sea during 1993–2007, *J. Geophys. Res.*, 115, C03012, doi:10.1029/2009JC005657.

Zhang, X., R. D. Hetland, M. Marta-Almeida, and S. F. DiMarco (2012), A numerical investigation of the Mississippi and Atchafalaya freshwater transport, filling and flushing times on the Texas-Louisiana Shelf, *J. Geophys. Res.*, 117, C11009, doi:10.1029/2012JC008108.

Zhao, H. (1990), *The Evolution of the Pearl River Estuary [in Chinese]*, pp. 1–357, China Ocean Press, Beijing.

Zu, T. T., D. X. Wang, J. P. Gan, and W. B. Guan (2014), On the role of wind and tide in generating variability of Pearl River plume during summer in a coupled wide estuary and shelf system, *J. Marine Syst.*, 136, 65–79.